MAJIS infrared performances during the JUICE 2024 Earth fly-by: comparisons with IASI measurements and detection of atmospheric trace species

Sandrine Guerlet[1,2], Raymond Armante[1], Ninon Lauzanne[1], François Poulet[3], Yves Langevin[3], Sébastien Rodriguez[4], Leigh Fletcher[5], Thierry Fouchet[2], Giuseppe Piccioni[6], and Alessandra Migliorini[7]

[1]Laboratoire de Meteorologie Dynamique, LMD-IPSL, CNRS, Sorbonne Université, Université PSL, Institut Polytechnique, Paris, France
[2]LIRA, Observatoire de Paris, Université PSL, CNRS, Sorbonne Université, Université Paris Cité, 92195 Meudon Cedex, France
[3]IAS, CNRS, Université Paris-Saclay, 91405 Orsay Cedex, France
[4]Université Paris Cité, Institut de physique du globe de Paris (IPGP), CNRS, Paris, France
[5]School of Physics and Astronomy, University of Leicester, Leicester, United Kingdom
[6]Istituto Nazionale di Astrofisica - Istituto di Astrofisica e Planetologia Spaziali (INAF-IAPS), I-00133, Roma, Italy
[7]Istituto Nazionale di Astrofisica - Astronomical Observatory of Padova, I-35122, Padova, Italy

Correspondence: Sandrine Guerlet (sandrine.guerlet@lmd.ipsl.fr)

Abstract. The JUpiter ICy moons Explorer spacecraft (JUICE) successfully performed a Lunar and Earth gravity assist maneuver on 19 and 20th August 2024, which provided an excellent opportunity to test its instruments before its arrival at Jupiter in 2031. Here we focus on the evaluation of the performances of the infrared channel of the Moons and Jupiter Imaging Spectrometer (MAJIS) based on Earth observations acquired over part of the Pacific Ocean at tropical latitudes. We specifically compare MAJIS observations with nearly co-located ones from the Infrared Atmospheric Sounding Interferometer (IASI). The two instruments overlap in the spectral range 3.6 and 5.56 μm. After filtering out spectra contaminated by clouds or ocean glint, and corrected for a small spectral shift in MAJIS data, we find a very satisfactory agreement (within $\pm$10% across most of the spectral range) between the absolute radiance of the two instruments. We show that part – but not all – of the residual differences can be attributed to minor atmospheric variations (temperature and/or water vapor) between the scenes, especially when the two datasets were taken more than 2 hours apart. Our best co-location case study, with IASI and MAJIS taken only 20-minutes apart, is used to highlight a low radiometric calibration bias for MAJIS pixels at the left edge, with an 8% lower radiance for MAJIS compared to IASI. Conversely, we report an estimate of a +4% positive bias at the right edge.

We then compare MAJIS to synthetic spectra generated with a radiative transfer algorithm, the OPerational version of the Automatized Atmospheric Absorption Atlas (4A/OP). The use of 4A/OP allows us to highlight the detection and give an estimate of a lower-bound sensitivity of MAJIS spectra to several trace species: methane (CH_4), nitrous oxide (N_2O), ozone (O_3) and carbon monoxide (CO). Based on the residuals between MAJIS and synthetic spectra, we estimate the signal-to-noise ratio to lie in the range 200–300, meeting nominal expectations. These excellent performances point to promising future jovian atmospheric observations.

1 Introduction

The Jupiter Icy Moons Explorer (JUICE), launched in April 2023, successfully performed a Lunar and Earth gravitational assist on 19 and 20 August 2024, which provided a unique opportunity to test the in-flight performance of its instruments. In this study, we focus on Earth observations acquired by the Moons And Jupiter Imaging Spectrometer (MAJIS, Poulet et al. (2024)). This hyperspectral imager is equipped with two spectral channels: one covering the visible and near-infrared (VIS-NIR; 0.5–2.35 µm) and the other covering the infrared (IR; 2.28–5.56 µm). During the fly-by, MAJIS recorded spectra of the Earth surface (primarily over the ocean) and atmospheric thermal emission and solar backscattered radiation over parts of East Asia and the Pacific Ocean (see Poulet et al. (2025) for an overall description of the Earth fly-by). Given the availability of multiple Earth-observing remote sensing satellites, we leveraged this opportunity to compare MAJIS spectra with those taken from the Infrared Atmospheric Sounding Interferometer (IASI, Phulpin et al. (2007)) at similar – although not identical – locations, local times and viewing angles. IASI records spectra of the Earth thermal emission and solar reflection in the range 3.6–15.6 µm and is renowned for its excellent performances in terms of absolute radiometric calibration, spectral calibration and signal-to-noise ratio. Indeed, IASI measurements have been themselves validated against ground-based observations (Armante et al., 2016) and are frequently used as a reference for cross-calibrating other remote sensing instruments (Larar et al., 2010).

Since MAJIS and IASI overlap in their spectral coverage between 3.6 and 5.56 μm, this paper focuses on the evaluation of the radiometric calibration of MAJIS' IR channel by comparing its measurements with near-coincident IASI observations. A key challenge lies in taking into account the differences in spatial and spectral resolutions: IASI has a spectral resolution roughly six times finer than MAJIS, while having a wider individual field of view. Additionally, discrepancies in spatial resolution, observation time, and precise location between the two datasets can lead to differences in cloud cover or glint (specular reflection) contamination, which require careful consideration and are addressed in this work. To interpret subtle differences between instruments, we employ the 4A/OP radiative transfer model (Scott and Chedin, 1981; Cheruy et al., 1995), which is also used to assess the spectroscopic calibration of MAJIS in a companion study (Langevin et al., 2026). Beyond calibration, as one goal of MAJIS is to retrieve and map the concentration of several trace species in Jupiter's atmosphere (e.g. water, ammonia, phosphine; see Fletcher et al. (2023)), we also use the Earth fly-by as an opportunity to evaluate MAJIS' detection capabilities for trace species in the Earth's atmosphere, specifically methane (CH_4), ozone (O_3), carbon monoxide (CO) and nitrous oxide (N_2O), relying on synthetic spectra generated with the 4A/OP model.

The paper is structured as follows: Section 2 details the characteristics of IASI and MAJIS observations, then Section 3 describes the 4A/OP radiative transfer code. Section 4 outlines the co-location and comparison methodology with IASI data, including cloud and glint contamination filtering. Section 5 presents the comparison of the two dataset and its implications for MAJIS' radiometric calibration. Section 6 continues on the radiometric calibration topic, but based on the comparison between two MAJIS swaths sampling the left and right parts of the detector array. Finally, Section 7 discusses the detection limits of MAJIS for trace species, followed by concluding remarks.

2 Characteristics of IASI and MAJIS observations

2.1 General characteristics, spectral ranges and resolution

IASI is a Fourier-Transform infrared spectrometer mounted onboard each of the three EUMETSAT Meteorological Operational satellite MetOp-A, B and C satellites launched respectively in 2006, 2012 and 2018. While the Metop-A instrument stopped operating in 2021, IASI remains operational on MetOp-B and C at the time of writing. Initially dedicated to the meteorological monitoring of atmospheric temperature, water vapour (August et al., 2012) and surface temperature (Capelle et al., 2022), IASI has demonstrated is capability to monitor also the atmospheric composition such as carbon dioxide, methane (Crevoisier et al., 2009, 2013), ammonia and halogenated species (Clerbaux et al., 2009). Additionally, IASI spectra enable the retrieval of spectral emissivity and aerosol opacity (Capelle et al., 2014). IASI's long-term operational record and high spectral resolution make it a benchmark for cross-calibration and validation of other infrared instruments.

MAJIS on the other hand is a two-channel (VIS-NIR and infrared) hyperspectral imager onboard the ESA JUICE mission, dedicated to characterizing Jupiter's atmosphere and the surfaces and exospheres of the Galilean satellites. Detailed characteristics of the MAJIS instrument and its science objectives can be found in Poulet et al. (2024).

IASI covers the thermal infrared spectral range from 645 to 2760 cm^{-1} (3.6–15.6 μm), whereas MAJIS spans 0.5–5.56 µm across its two channels. We will specifically focus on its IR channel, spanning 2.28–5.56 µm. Regarding spectral resolution, IASI's instrument response function has a full width at half maximum (FWHM) of 0.5 cm^{-1} (apodized), corresponding to $\sim$1.25 nm at 5 µm. This is approximately 5.5 times finer than MAJIS's FWHM of 6.86 nm in its infrared channel. In terms of resolving power (R) at 5 µm, this yields R $\sim$ 4000 for IASI and R $\sim$ 730 for MAJIS.

2.2 Field of views and viewing geometries

IASI's field of view (FOV) is composed of four (2×2) circular pixels with moderate spatial resolution, each individual pixel projecting to a 12 km diameter footprint on Earth, at nadir. In contrast, MAJIS offers extensive imaging capabilities: both channels consist in an 800-pixel-wide detector array. These pixels are binned 2×2, resulting in 400 nominal individual FOVs, each with an angular width of 150 µrad. However, the EGA MAJIS datasets used in this study are not 400 pixels-wide. This stems from the fact that the Earth is an exceptionally bright target for MAJIS (which is designed to observe colder bodies). To avoid saturation, integration times were reduced to 11, 22 or 70 ms (compared to the typical 800 ms planned for future Jupiter observations). These shorter exposures were obtained by limiting the instrument FOV to 64 or 128 out of the 400 nominal pixels. These pixels are either located at the left edge, middle part or right edge of the detector. When one edge of the detector was targeted, 15 pixels were positionned out-of-field of view on purpose to assess straylight contamination (significant only in the VISNIR channel, see Langevin et al. (2026)).

During the Earth Gravity Assist (EGA) of August 2024, MAJIS acquired 2-D images by stacking successive frames (across the slit) obtained by scanning its internal mirror. This resulted in 19 swaths, with dimensions spanning from 64×330 to 128×865 pixels (see Table 1 in Poulet et al. (2025) for the full list of swath with their exact dimensions). Given the Earth

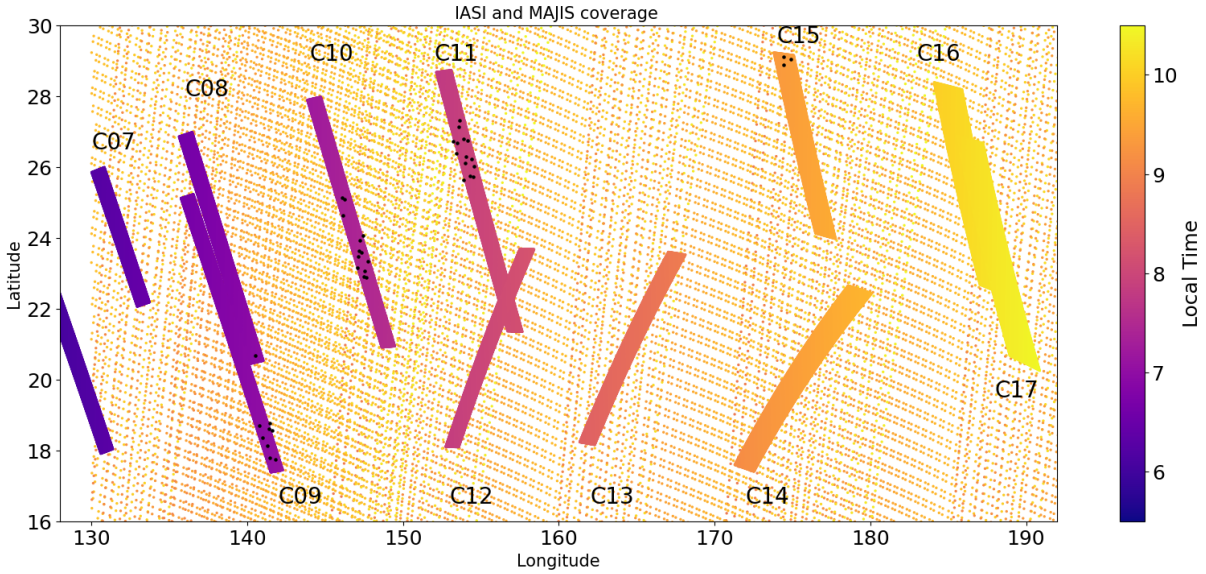


Figure 1. Projection of 11 MAJIS swaths out of the 19 taken during EGA on 20 August 2024, labeled from C07 to C17, coloured according to local time. All dots represent the locations of IASI data acquired that same day from MetOp-B and -C satellites for the morning pass (local time near ∼9:30). We already show in this plot, as black dots, the location of 39 IASI observations that pass all our quality and co-location filters (see section 4).

flyby conditions, at a distance of 6,840 km from Earth, each pixel projected to an instantaneous field of view (IFOV) of ∼1.3 km on the ground.

IASI does not have imaging capabilities per se. The MetOp satellites are on polar orbits and spatial coverage is obtained by scanning the IASI instruments across the satellite's tracks with a swath of ±48° around nadir. With an orbital period of approximately 2 hours, near-global coverage (at rather coarse spatial resolution) is reached in 12 hours. Furthermore, MetOp satellites are on Sun-synchronous orbits, limiting Earth observations around two local times centered at 9:30 and 21:30. In contrast, MAJIS Earth observations spanned approximately the local time range 3:00–10:30, and at emission angles from 0° (nadir) to 65° (see also Table 1 in Oliva et al. (2026) for full information on local times and geometries of all MAJIS Earth scans).

While 19 data cubes were acquired by MAJIS in the range of longitudes 80–190E, we have retained only 11 of them as a starting point to search for co-locations with IASI: we exclude the last two, acquired in near limb geometry, and do not show the results for 6 other cubes taken at longitudes west of 130°E as the local time difference with IASI was judged too significant (>4 hours). The 11 MAJIS data cubes selected at this stage were all acquired in early morning, between ∼6h00 and 10h30 and span latitudes 17–29° North and longitudes 130–190°E. On the IASI side, we gathered data from both IASI-B and IASI-C taken in this geographic area for the morning pass that same day. The spatial and local time coverage of both datasets is shown in Fig. 1, before any filtering is done.

3 Description of 4A/OP

4A/OP, standing for OPerational version of the Automatized Atmospheric Absorption Atlas, is a fast and accurate radiative transfer model developed jointly by the Laboratoire de Météorologie Dynamique (LMD), the French Centre National d'Etudes Spatiales (CNES) and Noveltis (see Dogniaux et al. (2021) and references therein). This model exploits precomputed optical thicknesses "Atlases" generated at a spectral resolution of 5×10^{-4} cm^{-1} for a range of reference temperature-pressure profiles representative of the Earth atmospheric variability. To calculate optical thicknesses, spectroscopic parameters are nominally provided from the latest version of the GEISA spectroscopic database (Jacquinet-Husson et al., 2016; Delahaye et al., 2021). Originally developed for the thermal infrared region, 4A/OP has since been extended to the shortwave infrared and visible ranges. This versatile model supports multiple observation geometries (nadir, limb, occultation), user-defined instrument response functions, up to 53 molecular species, and the possibility to include scattering by clouds and aerosols (Sic et al., 2026). Derivatives of the radiance with respect to temperature or mixing ratio of a species (Jacobians) can also be calculated. For example, 4A/OP is used for the daily retrievals of sea surface temperature and trace species from IASI and has been selected by CNES as the reference radiative transfer model for the development of the MicroCarb and MERLIN missions (Cassé et al., 2021).

In our study, we generate spectra in the thermal infrared part (2.5 to 5.56 µm for MAJIS; 3.6 to 15.5 µm for IASI) and neglect scattering. We consider only cloud-free scenes (see section 4.1) and thus omit emission and absorption by clouds. Data considered here were acquired over the ocean, where marine aerosols may be present but their extinction in the thermal infrared is negligible and is therefore not included. The ocean surface emissivity is set to a nominal value of 0.97 across the entire spectral range considered here, though sensitivity tests to this parameter are presented later. The radiative transfer code considers 43 vertical layers in plane-parallel approximation, ranging from just above the surface to an uppermost layer located at 2.5×10^{-3} hPa. Molecules considered in the radiative transfer calculations are :

- For MAJIS: H_2O, CO_2, O_3, N_2O, CO, CH_4, O_2, NO, HDO.
- For IASI: the above, plus SO_2, NO_2, C_2H_6, C_2H_2, NH_3 and three CFCs.

In addition, several continua and Collisional-Induced Absorption (CIA) emissions are taken into account (N_2, O_2, H_2O), as well as line-mixing effects for CO_2, CH_4 and H_2O.

Regarding the instrument response function, for MAJIS we assume a Gaussian profile with a nominal FWHM of 6.86 nm, as determined from ground-based spectral calibration (Haffoud et al., 2024), while the IASI FWHM is defined in wavenumbers units and set to 0.50 cm^{-1}.

An example of a IASI spectrum on its full wavelength range is shown in Fig. 2, along with a synthetic spectrum that we computed with 4A/OP. This example was chosen among the IASI-MAJIS co-located data discussed later. This synthetic spectrum was generated by setting the main parameters (surface temperature, atmospheric temperature, humidity profiles) to the Level 2 IASI data (EUMETSAT data products, August et al. (2012)). The ozone profile was set to that extracted from the ERA5 reanalysis for this time and location and was slightly scaled to match the ozone band at 9.6 µm. Other trace species were

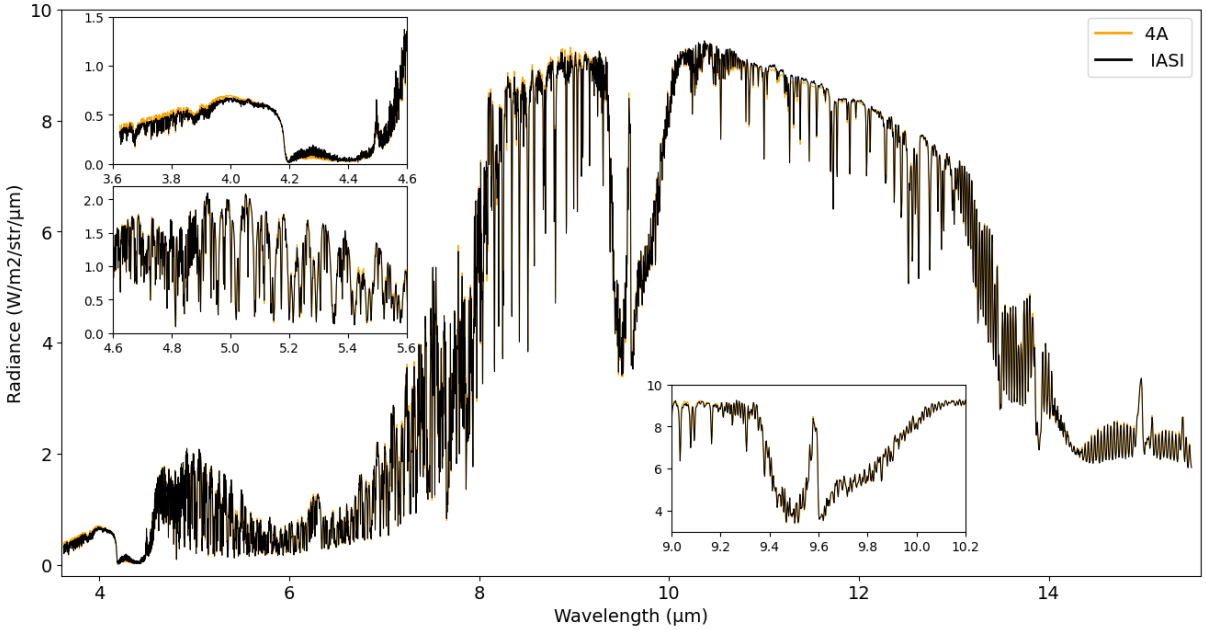


Figure 2. Example of a IASI spectrum acquired over the Pacific Ocean on 20 August 2024 (in black) along with a synthetic spectrum generated with 4A (orange). Embedded are three zooms, one centered at the 9.6 µm ozone band as a showcase of excellent agreement between model and observations, and two others covering MAJIS spectral range to highlight the complex spectral features in this range.

set to typical vertical profiles found in the tropics; however, some IASI-4A/OP mismatches were found in the spectral ranges corresponding to the signatures of CO, CH_4 and N_2O. We thus also scaled these trace species profiles (by less than 10%) until we obtained a good match of these spectral features, resulting in the spectrum shown in Fig. 2. This set of trace species profiles will serve as a basis for our sensitivity studies discussed in section 7.

The excellent agreement between the model (4A/OP) and the IASI observations shown in Fig. 2 vouch for the use of the 4A/OP radiative transfer model in our study. We note however that the synthetic spectrum underestimates the emission in the core of the 4.3 µm CO_2 band, which is a well-known shortcoming of several radiative transfer models (including 4A/OP) that do not take into account the complex contribution from non-LTE CO_2 emission, originating from the upper stratosphere. We also notice a small overestimation of radiance in the 4A/OP spectrum in the range 3.6–4.0 µm and 8–9 µm, and an underestimation of the observed radiance in the range 10–12 µm. This mismatch, here on the order of 0.05 W/m^2/sr/µm, is not systematic among the various IASI measurements we analysed. We suspect that it could be due to the assumption of a constant emissivity over the whole spectral range in our simulations, while the actual emissivity is slightly wavelength and viewing angle dependent.

4 Co-location method

4.1 Filtering for clouds

Before searching for co-located data, a first step is to filter out cloudy observations from both datasets. Indeed, the precise local time, location and size of the footprints of the two instruments being different, they could be contaminated by clouds in different ways. Clouds, located in the troposphere, are much colder than the surface and appear as a low radiance thermal emission. Even a small contamination by cloud will impact the outgoing emission spectra (see also Poulet et al. (2025); Oliva et al. (2026)). The brightness temperature (BT) near 3.9 µm or 4.6 µm serves as good proxy for cloud coverage in the thermal infrared, in particular above the tropical ocean where the surface temperature does not vary significantly over large areas. At these wavelengths, located in regions of small gaseous opacity, a low BT will indicate the presence of tropospheric clouds, emitting infrared radiation at cold temperatures. A map of the BT at 4.64 µm for both MAJIS and IASI observations is shown in Fig. 3, revealing cloudy areas. In particular, C16 and C17 were found nearly fully cloudy. A striking feature appears for MAJIS observations labeled 'C12', 'C13' and 'C14', that have much lower BT than the surroundings and than the crossing MAJIS observation labeled 'C11'. This cannot be explained by cloud cover; rather, these three MAJIS observations were acquired with a longer integration time (70 ms instead of 11 ms for the 8 other swaths considered here) and the signal saturates in parts of the interferogram. Due to non-linearity effects, this can cause both positive and negative artefacts in the resulting spectra, here impacting MAJIS spectra in the form of negative (and spectrally flat) anomalies in the range 4.5–5.2 µm. While these three data cubes appear for context in some figures, they will not be retained in the final selection of MAJIS-IASI colocated data.

To filter out for clouds, on the MAJIS side, we rule out spectra that have a brightness temperature at 4.64 µm lower than 290K. This threshold is justified by a visual inspection of the data in both the thermal infrared at 4.64 µm and in the visible at 0.7 µm, as shown in Fig. 4. Indeed, bright areas at 0.7 µm indicate the presence of reflective clouds on top of a dark albedo ocean, and are strongly correlated with low brightness temperatures. Examples of MAJIS spectra for cloudy or cloud-free pixels are shown in Fig. 5 to illustrate cloud contamination effect.

On the IASI side, level 2 data come with a cloud fraction value within the IASI footprint, estimated from a camera called the Advanced Very High Resolution Radiometer (AVHRR). Mounted onboard MetOp satellites, it operates at 5 different channels simultaneously in the visible and infrared bands with an instantaneous square field of view of about 1.1 km. It is used operationally by EUMETSAT to provide cloud coverage and has been found to perform very well over the tropics and mid-latitudes (Whitburn et al., 2022). We choose to keep IASI data with a cloud fraction less than 5%, which is small enough to not significantly affect the outgoing thermal emission (the associated error on the radiance in the 3.6 – 5.5 µm range is estimated to be of the order of 1%). In addition, we note that all IASI pixels flagged as cloud-free (meaning here $<5\%$ cloud cover) have indeed brightness temperatures higher than $\sim$290K at 4.64 µm, which supports our chosen threshold for MAJIS (see Fig. 6).

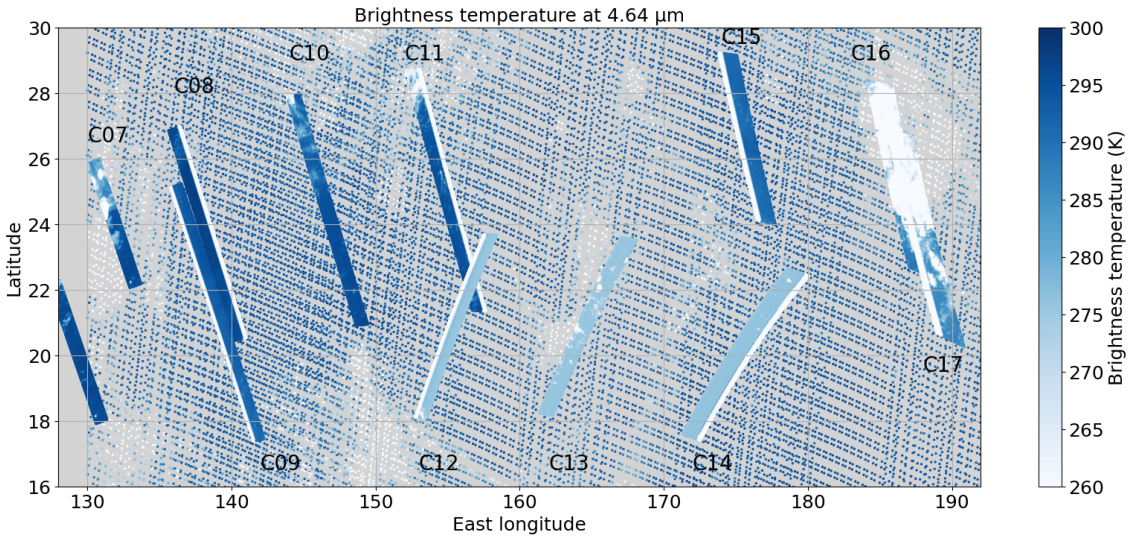


Figure 3. Map of the brightness temperature at 4.64 µm, used as a proxy for clouds, for 11 MAJIS swaths. All small dots represent brightness temperature for IASI observations (same color range). Each MAJIS swath shown here is 64 pixels wide and 330 to 690 pixels long. Several MAJIS swaths show a white stripe at one edge: they corresond to cases where the pointing was offset on purpose, with 15 pixels out-of-FOV, to evaluate straylight contamination. Labels are the same as those used in Oliva et al. (2026). Swaths labeled 'C12', 'C13' and 'C14' appear systematically colder due to a saturation effect (see text).

4.2 Effect and filtering of the glint spot

We further exclude, from our co-location analyses, IASI and MAJIS data contaminated by the specular reflection of the Sun over the ocean, which is called the glint spot. This occurs when the solar zenith angle is close to the satellite viewing zenith angle and is highly sensitive to the viewing azimuth angle. Because the ocean is not a smooth surface, the strength and direction of specular sunlight reflection depend on the orientation and slopes of the waves, which act as many small surfaces reflecting sunlight in a highly directionnal manner. A study of the Sun specular reflection signal in IASI observations can be found in Guérin et al. (2023), which reports on how the wind strength and direction changes the orientation of the wave facets, hence the strength of this signal. We further caution that two observations (one by IASI, one by MAJIS) can be very close in space and time, have similar viewing zenith angles, yet be affected very differently by solar specular reflection due to different azimuth viewing angles. Therefore, it is crucial to filter out glint-contaminated scenes within each dataset independently before comparing co-located spectra.

While the main contribution of this solar specular reflection is found in the visible and near infrared range (hence in the VIS-NIR channel of MAJIS), it also features a signature in the range 3.4–4 µm (see Fig. 7), where IASI and MAJIS NIR channels overlap. We therefore selected the 3.9 µm signal as a proxy for glint contamination in each dataset. At this wavelength, in the absence of cloud, the radiance should approximately correspond to the ocean surface temperature (typically 298–300K), assuming blackbody emission. When converted to brightness temperature (BT), however, the signal can reach values of up to

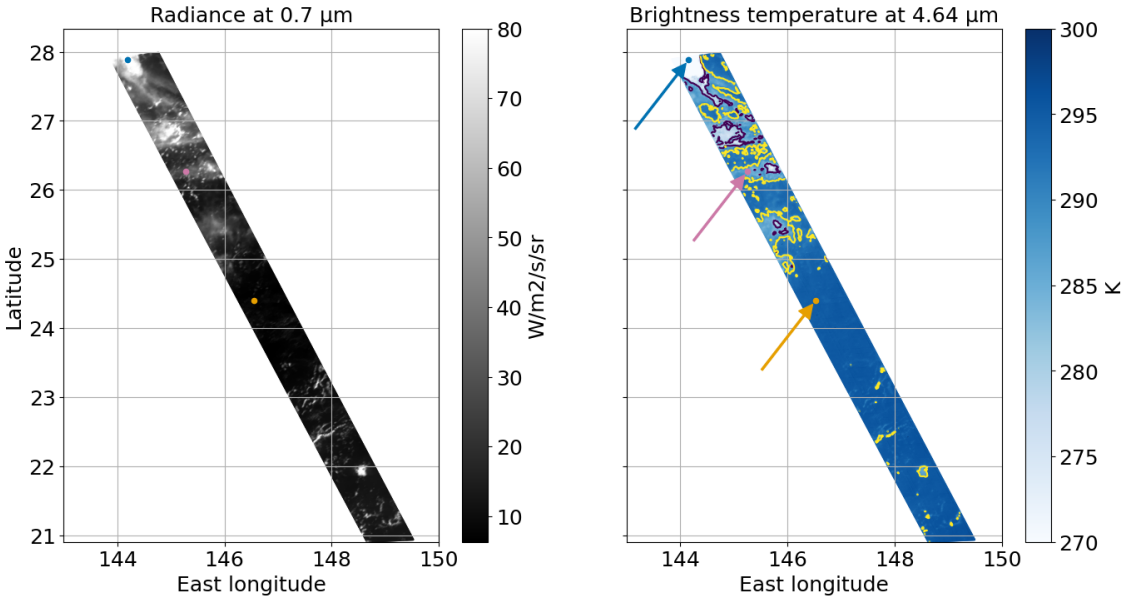


Figure 4. MAJIS radiance in the visible at 0.7 µm (left) and brightness temperature at 4.64 µm (right) for the swath labeled 'C10' in Fig. 3. On the right panel, the purple contour highlight BT values lower than 282K, the yellow contour BT values of 290K. Patches of clouds visible in the left panel are well identified by their low BT values in the right panel. Three dots (in green, red and orange) highlight three pixels which spectra are shown in Fig. 5.

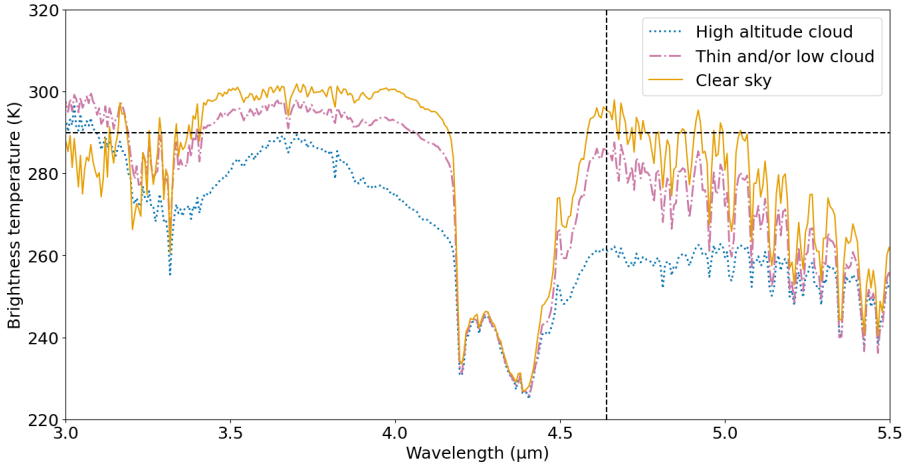


Figure 5. MAJIS spectra, in brightness temperature units, for three pixels from swath labeled 'C10' highlighted in color in Fig. 4. Dashed lines indicate the threshold value of 290K at 4.64 µm: spectra below this threshold are considered cloudy.

310K (see also Fig. 6 for IASI data), indicating the presence of additional non-thermal emission in the form of solar specular reflection.

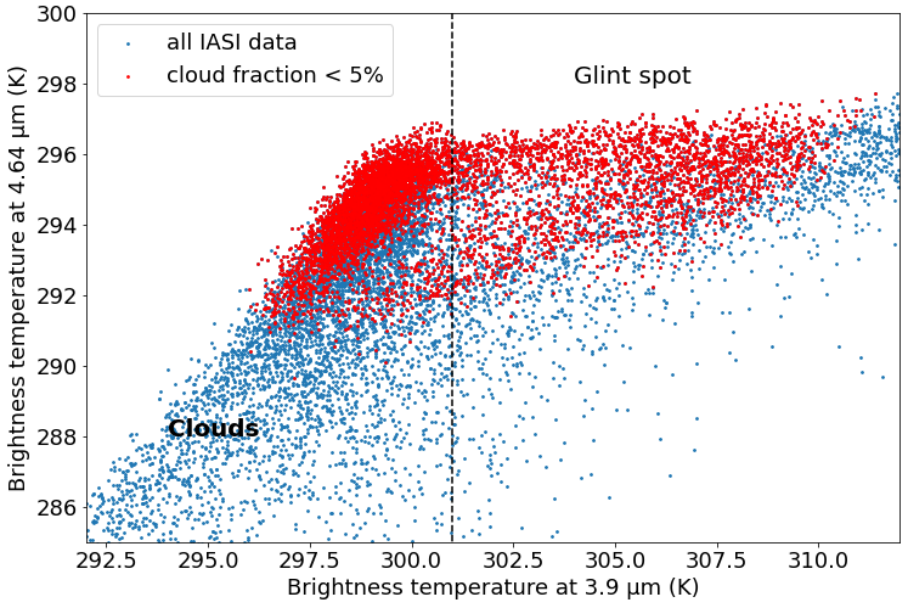


Figure 6. Scatter plot of the BT at 4.64 µm versus that at 3.9 µm for all IASI observations. Data colored in red have a negligible cloud coverage (less than 5%) within their field of view, as determined by an onboard camera. These nearly cloud-free observations are clustered near BT values of 292–297 K at 4.64 µm and 296–301K at 3.9 µm. The "tail" of high BT at 3.9 µm (>301K) represents observations with significant contribution from the specular reflection of the Sun (glint spot).

To select a threshold value above which we consider glint contamination to be too significant, we also investigated MAJIS data in the VIS-NIR channel. Here the glint signature is stronger as there is naturally more intense solar contribution. Since the ocean albedo is dark, any significant signal must be a reflection from a cloud and/or the glint spot. A map of MAJIS radiance at 2.35 µm is shown in Fig. 8 to illustrate this effect, revealing that parts of swaths 'C11' and 'C12' exhibit moderate glint contamination, while swaths 'C13' to 'C15' contain an even stronger solar specular reflection component. For example, swath labeled 'C15' was considered mostly cloud-free based on the BT at 4.64 µm but exhibits a non-zero radiance at 2.35 µm over a large part of its swath. This is consistent with the close values, for this data cube, of solar zenith angles (41°) and viewing angles (49°). In contrast, 'C08' and 'C09' are considered cloud-free and are also dark at 2.35 µm, hence not contaminated by glint.

Based on both the distribution of IASI BT at 3.9 µm and the correlation of MAJIS BT at 3.9 µm and radiance in the VIS-NIR channel at 0.7 µm (not shown) and 2.35 µm, we decided to filter out data with a BT at 3.9 µm greater than than 301K (see Fig. 6). This results in fitering out most MAJIS observations with a radiance signal greater than 0.25 $W.m^{-2}.sr^{-1}.\mu m^{-1}$ at 2.35 µm. We caution that this filter is not perfect, as it is based on a single wavelength and threshold value for all viewing conditions, and that residual glint contamination of the order of 2–3 % of excess radiance at 4 µm may still remain.

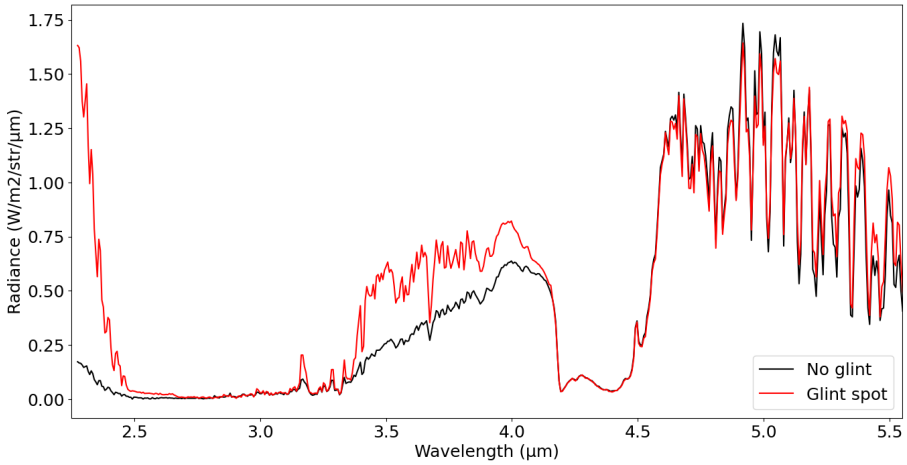


Figure 7. Example of two MAJIS spectra in the IR channel from swath labeled 'C15', inside (in red) and outside (in black) the glint spot.

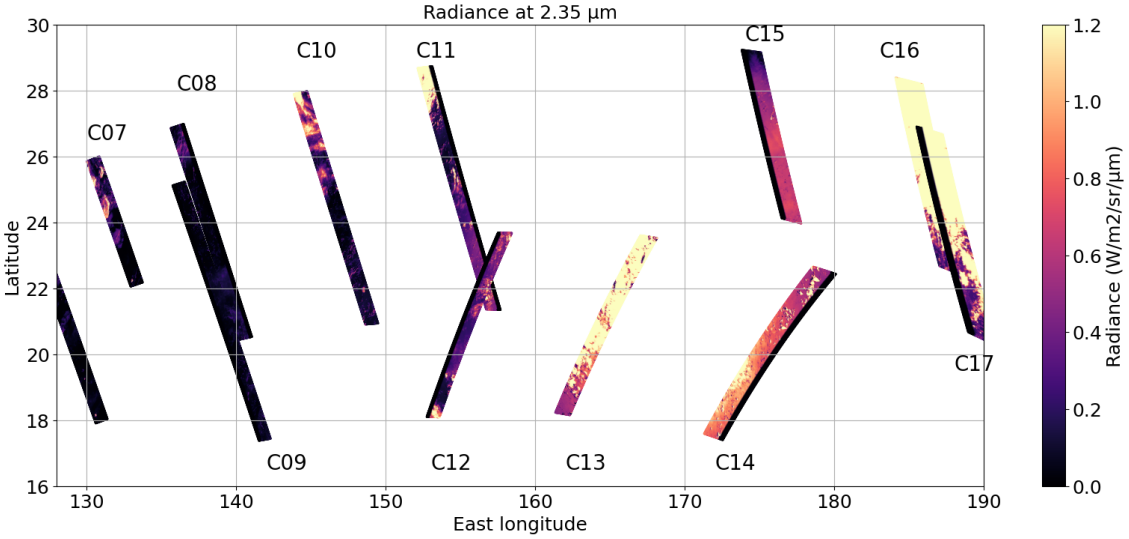


Figure 8. Map of the radiance at 2.35 µm from the VISNIR channel of MAJIS, capturing solar light reflected and backscattered by the surface and atmosphere. The ocean is very dark in the near infrared except in viewing geometries corresponding to the glint spot (specular reflection of the Sun) and/or in the case of reflection by clouds.

4.3 Co-location criteria and final selection

Once filtered for clouds and glint spot, we searched for IASI data co-located with MAJIS observations according to several criteria: spatial coincidence, temporal coincidence, and similar viewing angles. The most stringent criteria is the temporal one, as IASI observations are acquired around very specific local times (9:30 AM, 9:30 PM). We already showed in Fig. 1 the

Table 1. Summary of quality filters for IASI and MAJIS data, and co-location criteria.

Criteria	IASI	MAJIS
Cloud	$< 5\%$ cloud cover (camera)	BT(4.64 µm) > 290K
Glint	BT(3.9 µm) < 301K	
Diff. in emission angle	20°	
Diff. in local time	2.5 h	
Distance	MAJIS data within IASI footprint	

Table 2. Some characteristics of IASI and MAJIS co-located data, with θ_e the emission angle.

Swath number	Number of co-located IASI obs.	Longitude	Latitude	Local time (MAJIS)	Local time (IASI)	θ_e (MAJIS)	θ_e (IASI)
C08 (right)	1	140.5 - 140.6	20.6 - 20.8	6h57	9h23	19.3	37.3
C09 (left)	8	140.7 - 141.9	17.7 - 18.8	6h59 - 7h03	9h24 - 9h29	17.0° - 18.8°	25.5° - 33.3°
C10 (middle)	13	146.1 - 147.8	22.9 - 25.2	7h20 - 7h28	9h43 - 9h50	24.1° - 25.4°	4.9° - 10°
C11 (right)	14	153.2 - 154.6	25.6 - 27.4	7h50 - 7h58	9h18 - 9h23	32.4° - 33.7°	24.0° - 31.7°
C15 (left)	3	174.4 - 175.0	28.8 - 29.2	9h20 - 9h22	9h01 - 9h03	49.7° - 50.5°	52.2° - 53.8°

coverage of MAJIS and IASI observations (both from the MetOp-B and MetOp-C satellites) in terms of local times. We now further exclude entirely 'C12', 'C13' and 'C14' from our selection, due to saturation effects. In addition, 'C16' and 'C17' do not pass the cloud filter. Regarding the other swaths, initially setting a limit at ± 1 hour and a difference in emission angle of $\pm 10°$ retains only three IASI observations co-located with MAJIS data, exclusively over 'C15'. Indeed, as discussed in the previous section, most of this swath is contaminated by the glint spot, while the other swaths were taken earlier in the morning and further (in time) from IASI. We thus extended the criteria to ± 2.5 hours and $\pm 20°$ in emission angle and end up with 39 co-located IASI observations not contaminated by clouds nor the glint spot, represented in Fig. 1 as well as in zooms over swaths C9, C10, C11 and C15 in Fig. 9. The list of quality filters and co-location criteria are summarized in Table 1.

Each of these IASI observations is co-located with tens or even hundreds of MAJIS spectra. Indeed, for each IASI observation, we considered all MAJIS data contained into the much larger IASI field-of-view. The latter is a circle at nadir but is an ellipse elongated along the cross-track direction of MetOp orbital path, due to projection effects. Table 2 lists the local time and mean emission angle of co-located data for different MAJIS swaths. The two swaths for which we have the most co-located data are 'C10' and 'C11', corresponding to a local time gap of approximately 1h30 with IASI. The gap reaches our limit value (2h30) for swath 'C08', but is as low as 20 minutes for swath 'C15'. Note that different swaths correspond to different parts of MAJIS' detector array (left edge, middle, or right edge), as indicated in table 2.

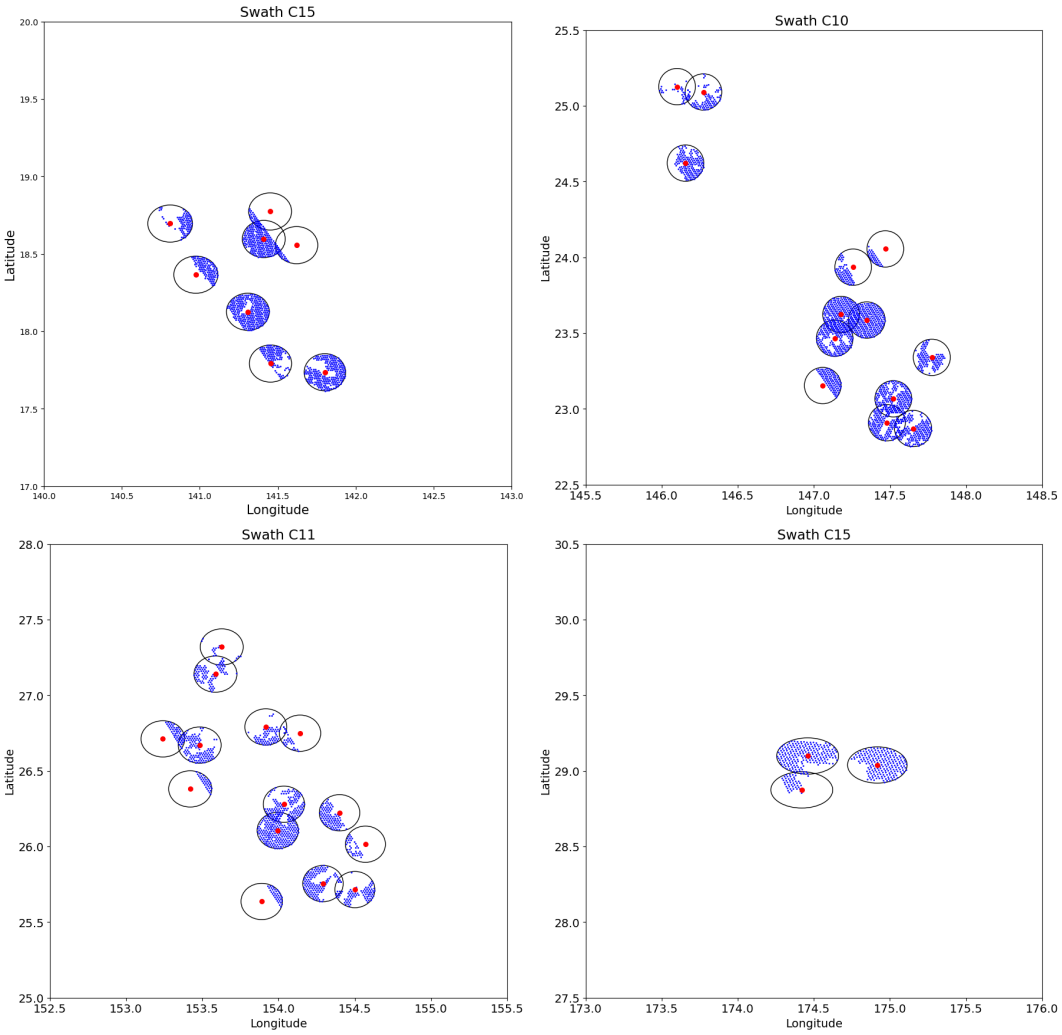


Figure 9. Projection of MAJIS observations (in blue) situated within the approximate footprint of co-located IASI observations whose central (latitude, longitude) are shown in red. The IASI footprint, outlined in black, is not a circle but an ellipse due to a projection effect.

5 Comparison of IASI and MAJIS spectra and implications for radiometric calibration

5.1 Preliminary remarks: spectral convolution and spectral shift correction

To quantitatively compare the two datasets, IASI spectra were convolved with the coarser 6.86 nm FWHM of MAJIS. To first order, this gives a very good match to MAJIS spectral features. However, this operation is not expected to yield a spectrum fully equivalent to a native MAJIS observation. Indeed, IASI spectra are already the result of a transformation process (Fourier-transform spectroscopy with its own instrument response function, including apodization at 0.5 cm^{-1} resolution), whereas MAJIS spectra are directly acquired at a fixed FWHM of 6.86 nm. We caution that convolving IASI spectra to MAJIS resolution

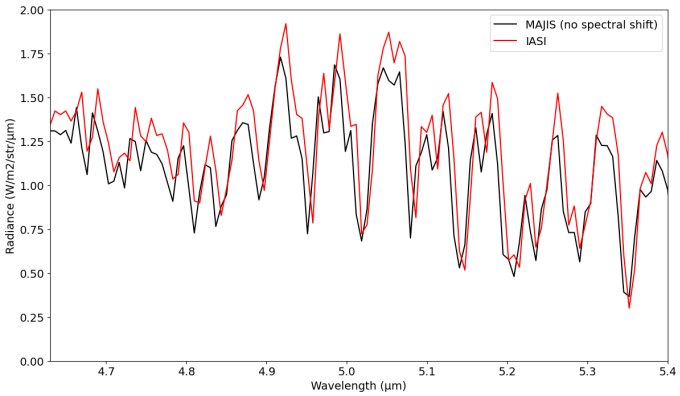


Figure 10. Comparison between a MAJIS spectrum (black) from swath C15 and a co-located IASI spectrum, convolved at MAJIS spectral resolution (red), highlighting a small spectral shift beyond 4 µm (a zoom between 4.6 and 5.4 µm is presented here for better visualization).

could therefore introduce small artifacts, as it neglects the intrinsic differences in how the two instruments sample the spectral domain.

In addition, this initial comparison revealed a small spectral shift between the two instruments at wavelengths beyond 4 µm, of the order of 4 nm (i.e., less than one MAJIS spectral bin). An example highlighting this shift is shown in Fig. 10. The same shift is also present in the MAJIS–4A/OP comparison. To precisely quantify it, cross-correlation applied to MAJIS and 4A/OP synthetic spectra was performed for different MAJIS swaths, and it was found that this shift varied from pixel to pixel along the slit. The details of MAJIS spectral calibration and the shift correction procedure are described in Langevin et al. (2026); here, we discuss results based on MAJIS spectra that have already been corrected for this spectral shift.

5.2 Statistics and trends over the 39 IASI co-located spectra

Considering the 39 co-located IASI observations, the median of the relative difference between IASI and MAJIS is found to be less than 5% over most of the spectral range (reaching 10% locally), centered near zero, with a 1-σ standard deviation ranging between 5 and 10% depending on wavelength (see Fig. 11). The exception is a "spike" seen near 4.2 µm corresponding to a minimum radiance in the spectra; the high relative difference found here is thus explained by the division by very small values. Note also that without the spectral shift correction, the IASI–MAJIS residuals are locally up to 20 times larger beyond 4 µm (not shown).

This first comparison thus indicates an excellent (ie. better than 10%) overall radiometric calibration of MAJIS. We noticed however different trends for the IASI–MAJIS difference depending on the considered MAJIS swath. For instance, the group of 8 cases showing the highest IASI–MAJIS residuals near 4.3 µm all belong to the same swath (C09), which has the largest local time difference with IASI ($\sim$2h30). At this wavelength, the radiance is strongly impacted by the lower stratospheric temperature. This suggests that the IASI–MAJIS residual at 4.3 µm reflect different atmospheric conditions (as will be shown in next section), more than resulting from a radiometric calibration bias. This raises a more general question: to what extent

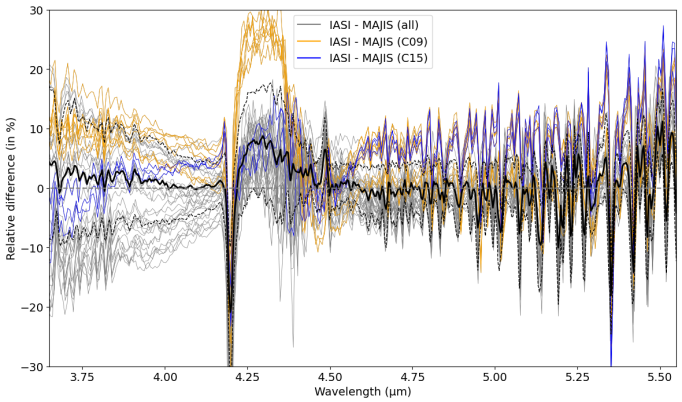


Figure 11. Assessement of the "IASI minus MAJIS" residuals. Each thin line is the relative difference, in %, between a IASI spectrum (convolved to MAJIS spectral resolution) and the mean of all MAJIS spectra co-located with that IASI observations (within IASI footprint). We highlight separately two swath: C09 in blue and C15 in orange. The thick black line represents the median of all IASI–MAJIS difference spectra, ± 1-σ standard deviation shown as dashed lines.

can the IASI–MAJIS mismatches be explained by differences in viewing geometry and geophysical conditions? We estimate these different effects in the next subsection.

We also notice different trends for the IASI–MAJIS difference depending on whether the MAJIS swath corresponds to the left, middle or right part of the array. The fact that the average IASI–MAJIS residuals are centered near zero could thus hide more subtle effects. In particular, the residuals are overall positive for swath C15 (corresponding to the left part of MAJIS detector) and negative for swath C11 (right part of the array). Hence, we must also consider the possibility of a pixel-dependent radiometric calibration bias (within the width of the array). This topic is adressed partly below and also in section 6.

5.3 Sensitivity studies to meteorological / surface conditions and viewing geometries

Starting from a reference synthetic spectrum computed with 4A/OP – obtained by setting the surface, atmospheric temperature and water vapor profile derived from the IASI L2 data – we computed additionnal synthetic spectra by varying one parameter at a time to evaluate the effects of:

- A $\pm$ 10% change in water vapor content;
- A $\pm$ 1K change in surface temperature;
- A $\pm$ 1K change in atmospheric temperature (assumed uniform over the vertical profile);
- A $\pm$ 0.01 or 0.02 change in surface emissivity;
- Replacing the MAJIS emission angle with the IASI one.

These values for water vapor and temperature were chosen according to ERA-5 hourly re-analysis extracted for 20th August 2024 in the same area, which shows that between 7AM and 10AM, atmospheric temperature varies by only 0.5K in the troposphere and up to 2–3K in the stratosphere, and water vapor by typically 10–15%.

The effects of these changes on the spectra are reported in Fig. 12, both in units of radiance and in percent, for the conditions of swaths C11 (right edge, ∼1h30 local time gap with IASI) and C15 (left edge, 20 mn gap). The orange line represents the impact of differences in emission angle between IASI and MAJIS and is to be interpreted as follows: if the two instruments were both perfectly calibrated and were looking exactly at the same place at the same time but with different viewing angles, we would expect the "IASI minus MAJIS" residuals to lie over the orange line.

Generally speaking, we report that small variations in atmospheric and surface conditions impact the spectra at the level of ±5% in radiance, which is commensurate with the spread of the IASI–MAJIS residuals over most of the spectral range. This highlights the need for strict spatio-temporal co-location critera in such an inter-instrument calibration exercice, as small changes in geophysical conditions can compromise data interpretation. However, some of the associated spectral signatures can be exploited and discussed.

Shortward of 4 µm, changes in surface temperature and emissivity impact the most the observed spectra. A change in emissivity of the order of +0.01 to 0.02, assuming a reference value of 0.97, could help bridge the gap between IASI and MAJIS for swath C11 and C15 by adjusting the slope in this spectral region, whereas changing other parameters results in spectral offsets (in % units). Note that for swath C10 (not shown), a change of emissivity of -0.02 is required to match IASI observations. Changes in emissivity can theoretically occur if the wind speed and direction changed enough to impact significantly the sea surface roughness between the ∼7:30–9:00 AM MAJIS observations and the ∼9:30 AM IASI ones. We caution however that modeling studies by Masuda et al. (1988); Masuda (2006) report emissivity variations of the order of 0.002 only, at 4 µm, due to wind speeds varying between 0 and 15 m/s. Emissivity is also expected to change with emission angles, but according to the same studies, the slight difference in emission angle between IASI and MAJIS are associated with negligible (< 0.002) variations in emissivity. Thus, the origin of the IASI–MAJIS residuals at wavelengths shorter than 4 µm remains unclear.

Sensitivity tests on atmospheric temperature reveals that a 1K temperature increase results in a 6–7% signal increase within the core of the 4.3 µm CO_2 band, sensitive to the (dry) upper troposphere and stratosphere, and a 3–4% signal increase beyond 4.6 µm, probing the lower and middle troposphere. The ∼25% IASI–MAJIS mismatch highlighted in Fig. 11 for swath C09, localized in the core of this CO_2 band, thus likely results from differences in stratospheric temperature of the order of 3 to 4K over a 2h30 local time difference, which is at the edge ERA-5 reanalysis and is therefore plausible. We further report that small (±10%) changes in water vapor content have a similar effect than a ±1K tropospheric temperature change beyond 4.6 µm, making it impossible to disentagle the two competing effects.

Interestingly, for swath C11 (and C10, not shown), we observe a correlation between the spectral features of the IASI–MAJIS residuals in absolute value and the impact of small temperature or water vapor changes in 4A/OP synthetic spectra, especially beyond 5 µm (see lower right panel of Fig. 12). Notably, even though the IASI–MAJIS residuals are slightly negative or centered around zero for swath C11 in this spectral range, the correlation is observed to be positive not with the negative

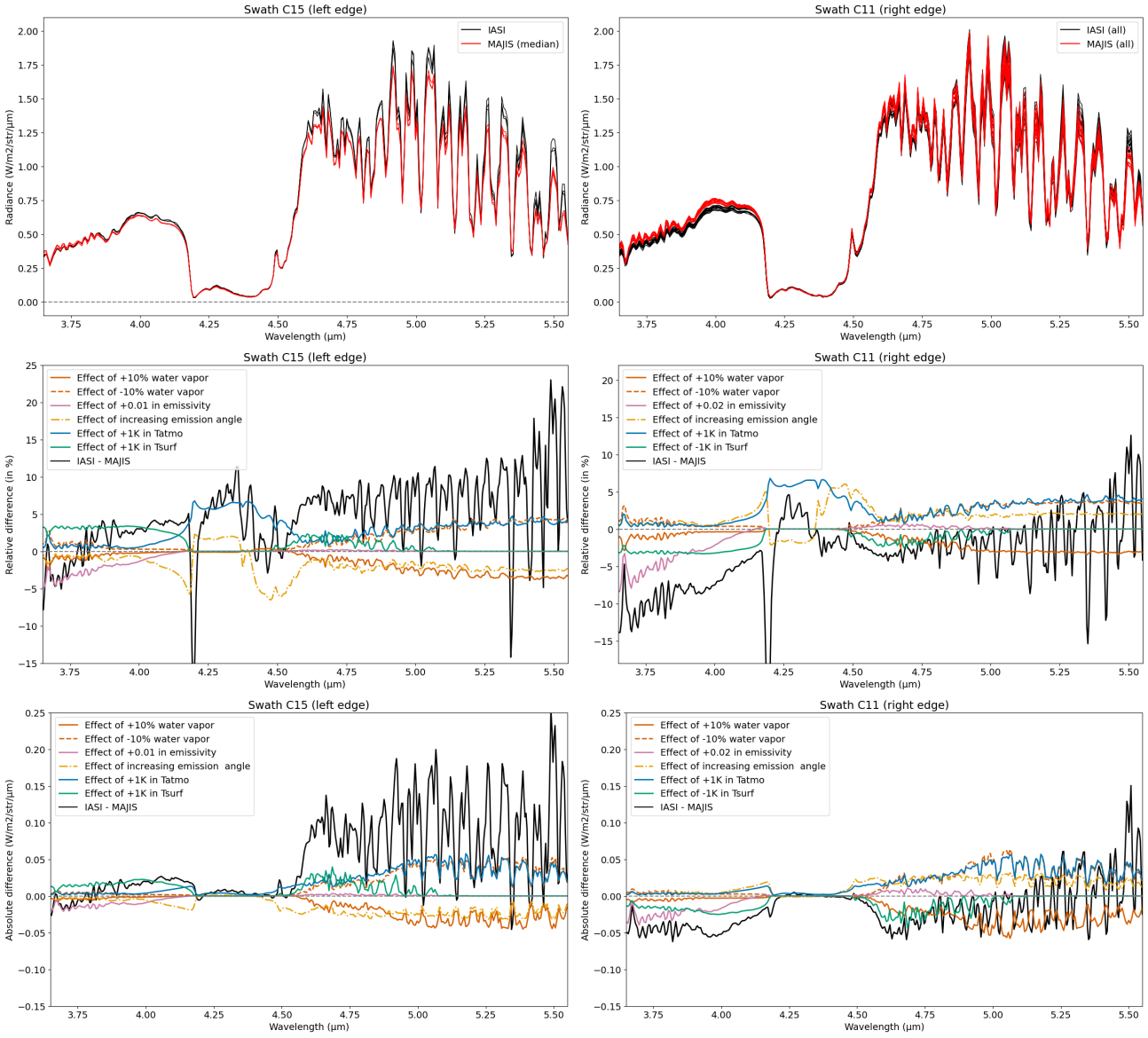


Figure 12. Top row: Comparison between IASI spectra convolved at MAJIS resolution (in black) and the mean of all MAJIS spectra located within the IASI footprint (in red). Second row: mean of the difference in % between IASI and MAJIS co-located spectra. Other lines (colored, dashed and dotted) represent the expected effects of small changes in atmospheric or surface temperature, water vapor content, surface emissivity or emission angle, as computed from synthetic spectra with 4A/OP. The strong spike near 4.2 µm in the left column, in % unit, results from near zero radiance at this wavelength (division by very small values). Third row: Same, in absolute radiance units. Fourth row: Same as third row, but applying a correction to MAJIS spsectra. The left column is for swath C15, the right column for swath C11.

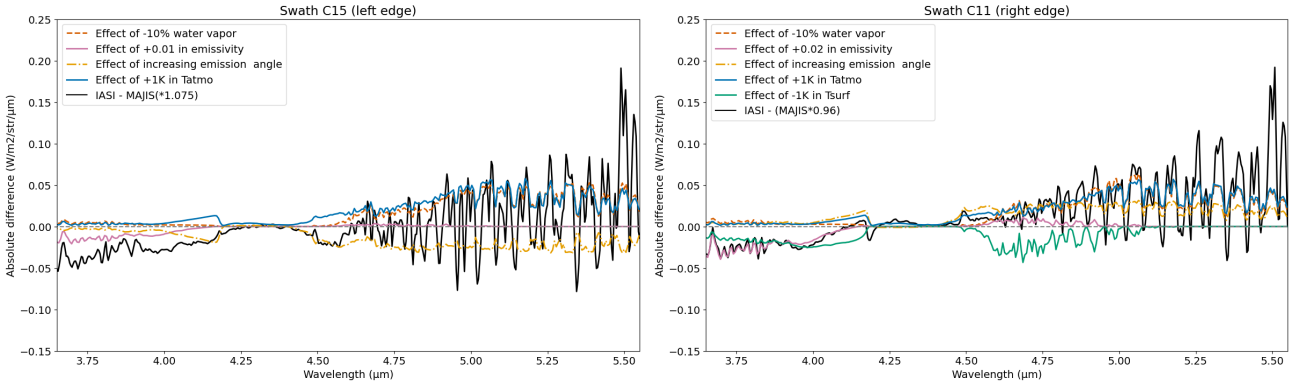


Figure 13. Same as third row of Fig. 12, but applying a tentative correction to MAJIS spectra of +7.5% from swath C15 and -4% to data from swath C11.

spectral signatures of a temperature decrease (or water vapor increase), but with that of a temperature increase (or water vapor decrease) (compare the black and blue spectra in the lower right panel of Fig. 12). Hence, a combinaition of a radiometric calibration bias and small differences in tropospheric temperature and/or water vapor could alltogether explain the IASI–MAJIS difference over the 4.6–5.56 µm region. Indeed, for C11 specifically, we find that assuming and correcting a $\sim$4% positive radiometric calibration bias of MAJIS reduces the IASI–MAJIS mismatch (χ^2 divided by two) and would bring the residuals close to the orange line, which represents the theoretical effect of the slight emission angle difference between the scenes (see Fig. 13). These residuals still correlate with water lines, indicating the remaining influence of temeporal changes in atmospheric conditions.

Last but not least, we note that the observed inter-instrument bias cannot be explained by the difference in emission angle alone, as radiative transfer simulations with 4A/OP predict a correction of opposite sign (eg., a mostly negative effect for swath C15 while the IASI–MAJIS residuals are mostly positive). Actually, in the case of swath C15, the IASI–MAJIS residuals in % units seem to follow the effect of accounting for different emission angle, but with a constant offset (compare the black and dot-dashed yellow curve in Fig. 12), and is a clear hint of a radiometric calibration bias. Invoking a constant -7 to -8% bias in MAJIS radiance measurements would divide the χ^2 by four (see Fig. 13). In this case, only three co-located IASI spectra matched our co-location filters, but as they were acquired within 20 minutes of the MAJIS observations, we can reasonably assume that differences in geophysical conditions play a minor role. The assessment of this radiometric bias is derived more precisely in section 5.4.

5.4 A more detailed investigation of the IASI-MAJIS residuals for swath C15

Below, we employ an intercomparison methodology that directly accounts for the small difference in emission angle. We compare in Fig. 14 a IASI spectrum at its native spectral resolution with a 4A/OP synthetic spectrum computed using the IASI instrument response function, and similarly for MAJIS. By not convolving IASI spectra to the MAJIS spectral resolution,

we avoid potential artifacts, as mentioned in section 5.1. The two synthetic spectra are computed for the same geophysical conditions, but with the viewing angle corresponding to the respective IASI or MAJIS scene.

Instead of directly comparing MAJIS and IASI observations, we now compare the difference between the two "synthetic minus observed spectra" residuals (the IASI residuals minus the MAJIS residuals). We note that "spikes" are visible in the MAJIS–4A/OP difference, especially beyond 5 µm, some of which visible in the IASI–4A/OP residuals as well. They could be due to errors in the forward model (ie. water vapor and/or atmospheric temperature profile; spectroscopic errors...) and/or to a misrepresentation of MAJIS instrument response function, such as a wavelength-dependent FWHM (see Langevin et al. (2026) for more investigation on this topic); but that does not alter our conclusions. Indeed, the goal here is not to discuss the observation-model residuals for each instrument individually, but to focus on the inter-instrument residuals. This method has the advantage of cancelling out errors in the forward model. The difference between (4A/OP – obs)$_{IASI}$ – (4A/OP – obs)$_{MAJIS}$ reveals a rather wavelength-independent offset between the instruments, with MAJIS showing on average 7.5% less flux than IASI observations between 4 and 5.3 µm, increasing to 10% beyond 5.3 µm. This is consistent with our previous estimate of a negative bias for swath C15, as discussed above.

The same exercise was done for other swaths but it did not indicate calibration offsets as clearly as for swath C15, due to the larger local time gap between instruments and the growing influence of changes in surface and atmospheric conditions. It did support our assumption of a *positive* bias in MAJIS for swath C11 though. One way to reconcile these two findings is if calibration errors depend on the pixel position on the detector array, as swath C15 corresponds to the left edge of the detector, and swath C11 to the right edge. This is adressed in the next section.

6 Radiometric bias within the MAJIS slit and summary of radiometric bias estimates

To investigate this hypothesis, we closely examined the case of swaths C08 and C09, which were acquired in close succession, with the two swaths touching each other and taken at the opposite edges of the MAJIS array (as best seen in Fig. 3 and zoomed in in Fig. 15). Figure 15 reveals a clear higher radiance in swath C08, which corresponds to the right edge of the detector (like C11), compared to C09 (the left edge, like C15). The local time difference was only $\sim$3 minutes, and the emission angles differed by only 3°, which should both have negligible impact on the measured radiance. The higher radiance in C08 compared to C09 is almost constant between 3.5 and 4.9 µm, amounting to 13%, and decreases (to a minimum of 5%) at other parts of the infrared spectrum. This result is consistent with our previous finding of a positive bias of the order of $\sim$4% for MAJIS data from C11 (right edge, like C08) relative to IASI, and a $\sim$-7.5% negative bias for swath C15 (left edge of the detector).

We conclude that over the spectral range 4–5.3 µm, small calibration biases ranging from approximately +4% to -8% between MAJIS left and right edges are found. This is most solidely based on the comparison with co-located IASI data taken at close local times (swath C15) and based on MAJIS (left edge)–MAJIS (right edge) comparison. Shortward of 4 µm, IASI–MAJIS mismatches in the range $\pm$ 10% are also observed but are less clearly tied to calibration biases. Given the greater local time gap (>2h) with IASI for the C10 observation sampling the middle part of the MAJIS array, no robust quantitative estimate of a radiometric bias was done for that part.

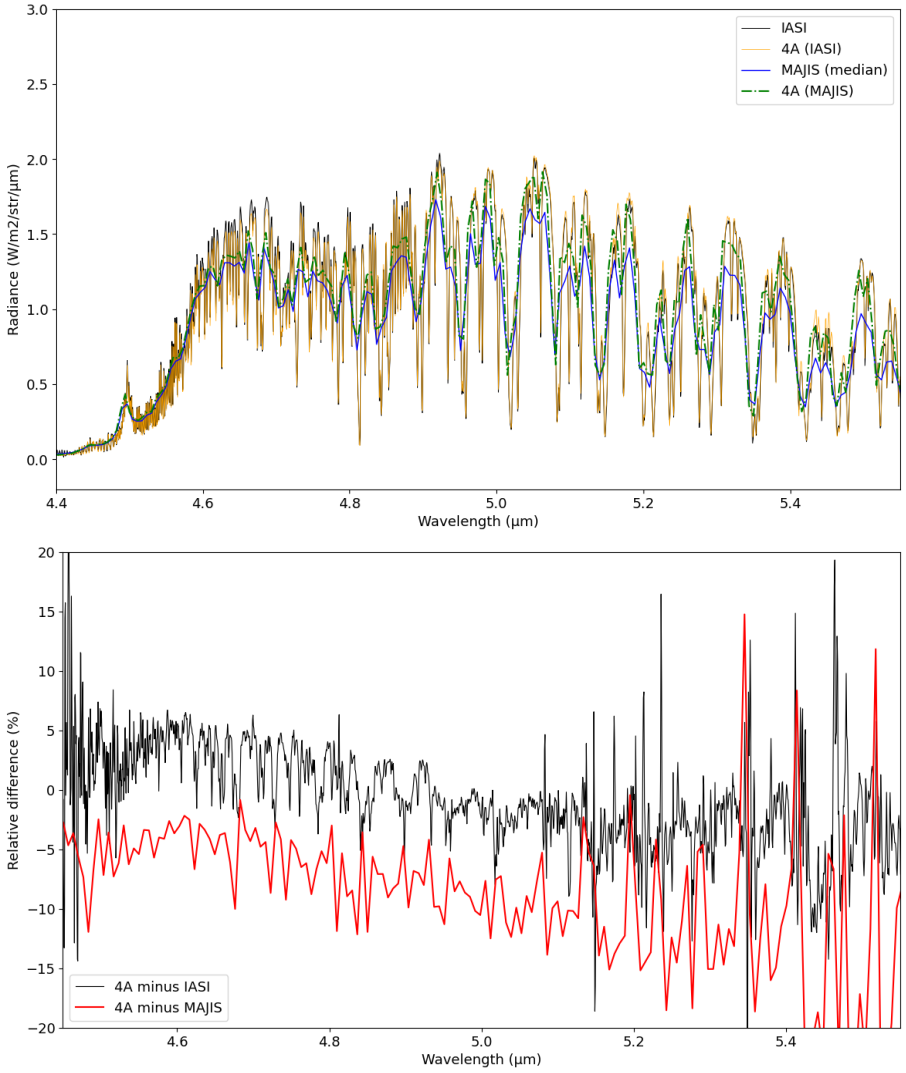


Figure 14. Top: Comparison between a IASI spectrum at its native resolution (black), a 4A/OP spectrum for the same viewing conditions and IASI instrument lineshape function (ILS) (orange); a MAJIS spectrum (in blue) and a 4A/OP spectrum for the same geophysical conditions as the orange one but MAJIS' ISL and viewing conditions (dashed green). Bottom: Comparing the (4A/OP – observation) difference for IASI (black) and MAJIS (red), in percent: the two curves are offset by ∼7.5%.

7 Comparison with synthetic spectra and sensitivity to trace species

Having carefully assessed the agreement with IASI observations, we now turn to the detection of (and study of the sensitivity to) several trace species in MAJIS IR spectra: ozone, carbon monoxide, nitrous oxide and methane. To do so, we selected a pair of one IASI and one MAJIS individual measurement from our swath 'C15'. We then defined a reference scenario

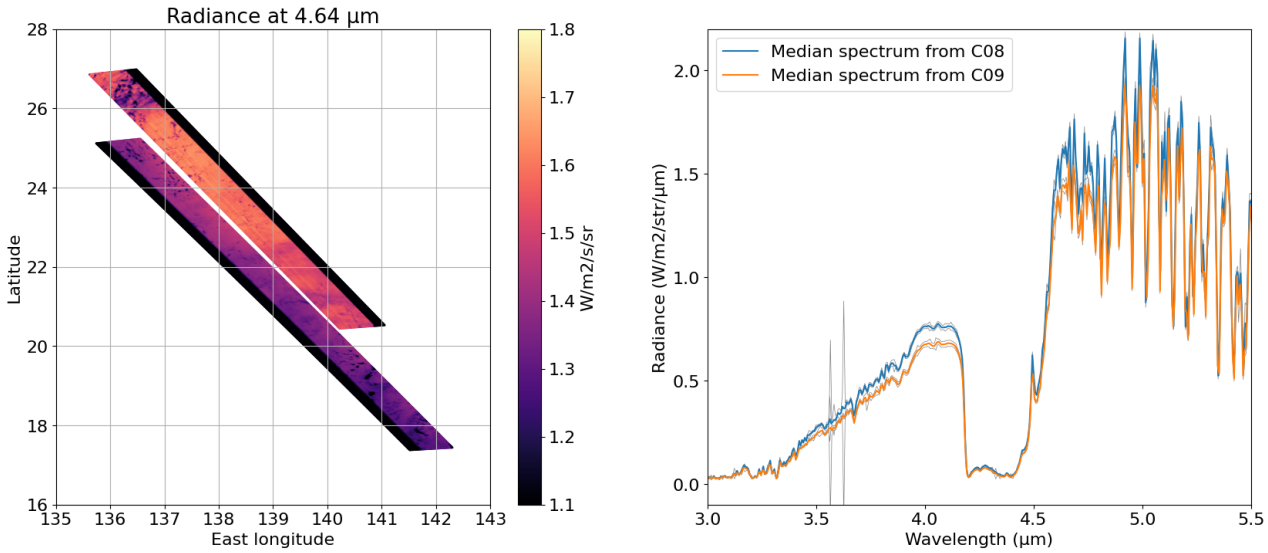


Figure 15. Left: Comparison between radiances at 4.64 µm from swath C09 (lower left swath) and C08 (upper right swath). The right panel shows a comparison between the median of spectra ($\pm 1 - \sigma$ standard deviation, in grey) acquired from swath C08 or C09 between 22 and 23° latitude, after cloud filters have been applied. The difference in emission angles is only 3° between the two spectra and cannot account for their mismatch.

(surface temperature, atmospheric temperature and composition vertical profiles) that best matches the IASI observation when computing the corresponding synthetic spectrum with 4A/OP. This reference atmosphere, based on the IASI L2 data, was already presented in section 2, along with the corresponding synthetic spectrum. We then computed another synthetic spectrum with the same surface and atmospheric conditions but for MAJIS spectral coverage and resolution. Hence, without running a retrieval, this method is expected to yield an excellent match to the MAJIS spectrum – when a 8% bias correction is applied. The noise level was first roughly estimated from the variance of the residuals (MAJIS minus 4A/OP), excluding the core of the 4.26 µm CO_2 band where 4A/OP underestimates the radiance due to lack of non-LTE emission in the model. Signal-to-noise levels of the order of 200 to 300 are obtained, which is in the same range as the estimates given in Poulet et al. (2025) based on read-out noise properties. Note that similarly to the IASI-MAJIS comparison, the match between 4A/OP and MAJIS is poorer beyond 5.4 µm. We then successively generated similar spectra but without the contribution of a given trace species. We find that methane is detected to the level of 6 times the 1-σ noise level, carbon monoxide to 4 times the noise level, ozone to 15 times the noise level, while nitrous oxide well exceeds these values (see Fig. 16).

To go further we then computed the Jacobians, which here are defined as the derivatives of the radiance at a wavelength λ_i with respect to a change of 10% in concentration of a given trace species at an altitude z_j (see Fig. 17). This allows for the determination of atmospheric layers for which the spectra have the greatest information content. This shows that we have the largest sensitivity to tropospheric N_2O, with a maximum sensitivity peaking at 500 hPa (∼5km altitude); followed by stratospheric ozone, peaking at 30 hPa (∼25–30 km altitude), while CO and CH_4 have a smaller absolute contribution and a

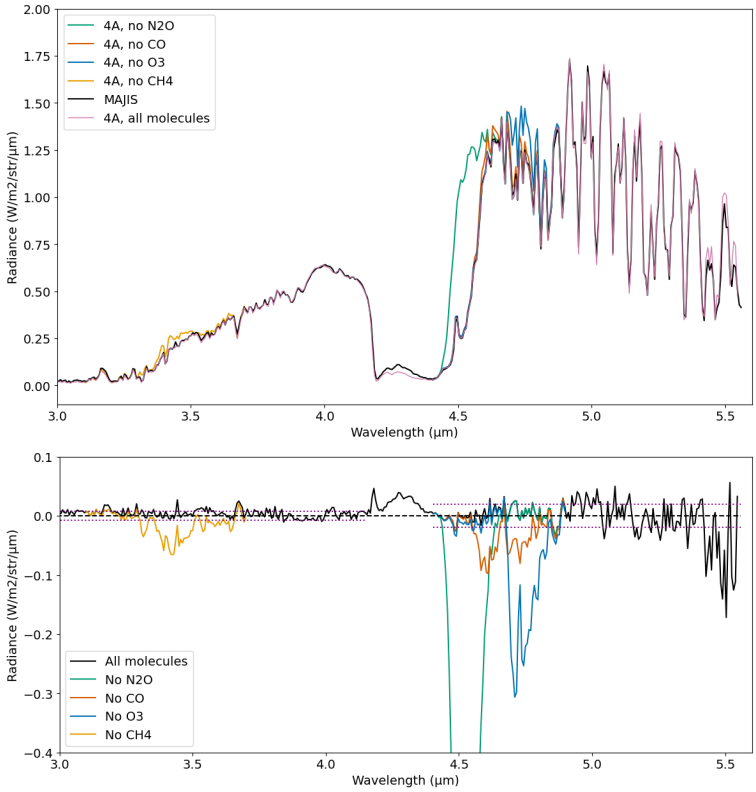


Figure 16. Top panel: Synthetic spectra generated with 4A/OP (color lines) compared to a MAJIS observation (in black), highlighting the sensitivity to several trace species. The bottom panel displays the residuals (MAJIS - 4A/OP). Estimate of the noise level in two spectral regions are displayed as dotted purple lines.

broader peak in the troposphere (2–10 km). The Jacobians are negative : an increase in a trace species abundance will lead to a more pronounced absorption feature on top of the background (warmer) surface and lower atmosphere thermal emission. From these Jacobians, we then computed the derivatives of the measurements to the total column of the trace species, which we call K_C. From the noise level at a given wavelength, σ_i, we can then compute the sensitivity σ_C on the total column of each traces species that we can get from the measurements:

$$\sigma_C = \left(\sum_i \frac{K_{C,i}^2}{\sigma_i^2} \right)^{-\frac{1}{2}} \quad (1)$$

The sum is done over the wavelength range of a given emission band. Note that our actual sensivitity would be to a partial column, as shown from Fig. 17. In addition, these estimates are “lower bound” values as the actual uncertainty would account for the propagation of several sources of errors (eg. on the temperature profile, ground emissivity,...) and for the correlation of errors between trace species.

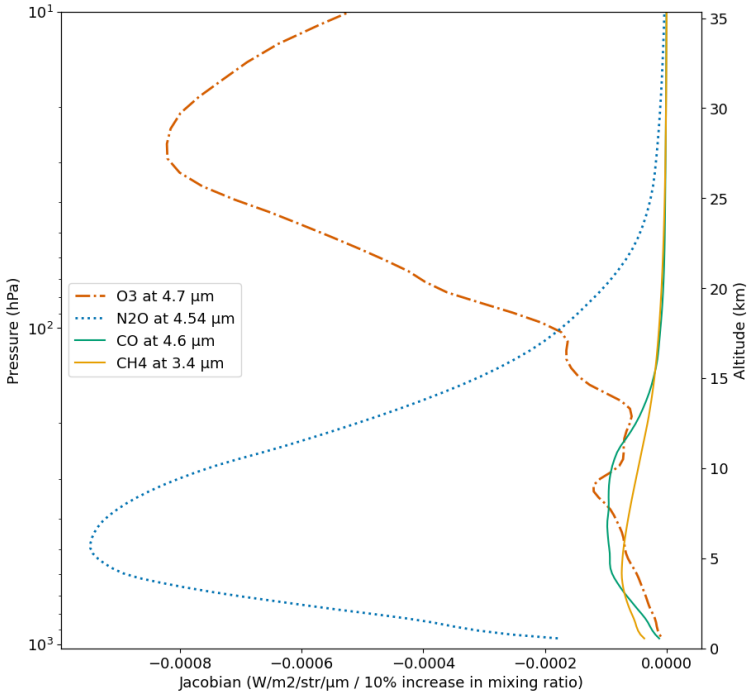


Figure 17. Impact on the radiance at a given wavelentgh (see label) to a change of 10%, at a given pressure level, in the mixing ratio of ozone (in red), nitrous oxide (blue), carbon monoxide (green) and methane (orange).

Results are summarized in table 3 in terms of a fraction of the column. Based on MAJIS noise level, we find that the minimum uncertainty on the methane column is 14%, which is well above the typical observed column variations for this gas, which amount to $\sim$5%. Hence, no useful information on the CH_4 spatial variations can be derived from MAJIS spectra, which was expected : this methane band at 3.4 µm is scarcely used in Earth remote sensing owing to a low infrared signal at this wavelength in nadir, and passive, remote sensing observations (it is however exploited in limb geometry or with active, LIDAR techniques). A similar uncertainty is reached for carbon monoxide, which has a weak signature. Our greatest sensitivity is to N_2O that can theoretically be derived with a 2.5% error on its column followed by ozone, where we estimate our sensitivity to its integrated column to 5%. All these molecules are mapped with IASI with better sensitivity owing to its higher spectral resolution and broader spectral range; ozone being retrieved from its strong 9.6 µm band from IASI spectra.

While the near infrared spectrum of the Earth is dominated by water vapour and carbon dioxide, on Jupiter, MAJIS spectra will be dominated by methane bands followed by ammonia, water and phosphine absorption. It is not possible to link our estimates on the precision level of a given trace species on Earth to future jovian measurements, given the very different gaseous composition, clouds and haze properties between the two planets. We refer the reader to Grassi et al. (2010) who evaluated at depth the performances (in terms of sensitivity to trace species) of the Jupiter Infrared and Auroral Mapper (JIRAM) instrument onboard Juno, an imaging spectrometer similar to MAJIS.

Table 3. Summary of the sensitivity study on trace species, based on the Jacobians and estimated noise level: peak altitude of the Jacobian, minimum uncertainty on the column abundance, in % ($\sigma_C/column * 100$), typical volume mixing ratio at this altitude, for the tropics, and typical range of observed variability.

Molecule	peak altitude	uncertainty	typical concentration	typical variations
CO	3–10 km	14%	100 ppbv	20%*
O_3	25–30 km	5%	275 Dobson units	10%
N_2O	3–8 km	2.5%	325 ppbv	3%
CH_4	2–8 km	14%	1.8 ppmv	5%

* locally up to 250 ppbv, hence 100% variation and more, over forest fires.

8 Conclusions

In this paper, we have evaluated the quality of MAJIS spectra acquired in the infrared channel during the 2024 JUICE Earth fly-by using co-located observations from IASI and a forward radiative transfer model, 4A/OP. The two instruments overlap in their spectral coverage in the range 3.6–5.56 μm; IASI having a ∼six times better spectral resolution but a ∼ten times larger spatial footprint. Our co-location method filters for cloud contamination and solar specular reflection (glint spot). From both the IASI–MAJIS and 4A/OP–MAJIS comparison, we report a small spectral shift of the order of 4 nm, documented in more detail in Langevin et al. (2026). As shown in section 5, differences in atmospheric conditions as small as ± 1K in temperature or ± 10% in water vapor content between data sets impact the quantitative analysis of the comparison. Therefore, strict temporal co-location criteria need to be applied to interpret the IASI–MAJIS difference in terms of radiometric calibration bias.

Considering the three IASI observations presenting the smallest local time gaps with MAJIS (20 minutes), we find that the IASI–MAJIS residuals can be attributed in large part to a radiometric calibration bias for MAJIS, of approximately -8%. This was based from data from the left edge of the MAJIS detector. We further report a bias between the left and right edge of the detector array, estimated to ∼12% (the right edge having a radiance ∼ 12% higher than the left edge). This implies an absolute radiometric bias of the order of +4% for the right edge, consistent with other IASI–MAJIS comparisons. These calibration biases were best evaluated over the 4–5.3 μm range. Outside this range, residual IASI-MAJIS mismatches reaching ± 10% were less clearly tied to calibration biases and additional data is needed.

Despite the challenges of inter-instrument comparisons, we can conclude that calibration biases of MAJIS are smaller than ±10% on a large part of the spectral range overlapping with that of IASI, with the caveat that MAJIS radiances present a small pixel-dependent bias. The JUICE Earth fly-by of September 2026 will bring complementary constraints on this issue so as to improve the calibration pipeline.

A signal-to-noise ratio of MAJIS in the range of 200 – 300 during Earth observations was evaluated by using the 4A/OP radiative transfer model together with a reference state of the atmosphere (partly coming from IASI Level 2 data) so as to compute a synthetic spectrum that best matches the MAJIS observations. This result is in line with the evaluations of SNR during ground-based calibration (Poulet et al., 2025). Several trace species (ozone, methane, carbon monoxide and nitrous

oxide) are clearly detected in MAJIS spectra, although with limited sensitivity. Carbon monoxide variations over forest fires and biomass burning regions could be detected by MAJIS during the Earth fly-by in September 2026 with a sub-spacecraft track crossing parts of Africa.

The main take home message from the analysis of the Earth fly-by MAJIS data in August 2024 is that the MAJIS radiometric calibration is reliable up to 10% and that the MAJIS noise level during Earth observations is in line with the performance model. This gives confidence that the characterization of trace species in the atmosphere of Jupiter will meet expectations during the JUICE science phase (2031 – 2035). Through these measurements (eg., ammonia maps), we expect MAJIS to bring valuable new constraints to the tropospheric dynamics and meteorological activity of the atmosphere of Jupiter.

Data availability. MAJIS calibrated data acquired during the JUICE Moon–Earth flyby in August 2024 are available through the following Guest Storage Facility: European Space Agency, 2026, ESA-JUICE_LEGA-Special-Issue_v1.0, https://doi.org/10.57780/esa-2bb387d .

Author contributions. SG led the study, wrote the paper, performed most of the comparisons with IASI observations and the radiative transfer calculations. RA provided the IASI data, developed the radiative transfer algorithm 4A/OP and contributed to the data analysis. NL contributed to the data analysis and visualization. FP, YL and SR participated in the discussion of the results. All authors reviewed and edited the manuscript.

Competing interests. The authors have no competing interests to declare.

Acknowledgements. French participation to this work on MAJIS data analysis was supported by the Centre National d'Etudes Spatiales (CNES). The Italian participation to JUICE mission is funded by the Italian Space Agency (ASI). In particular, this work has been developed under the ASI-INAF agreement n. 2023-6-HH.0. The Jupiter Icy Moons Explorer is a mission under ESA leadership with contributions from its Member States, NASA, JAXA and the Israel Space Agency. It is the first Large-class mission in ESA's Cosmic Vision programme. IASI has been built under the responsibility of CNES. The authors thank EUMETSAT for providing IASI data through EUMETCast service, and the AERIS data infrastructure for data processing (https://www.aeris-data.fr/). LMD particularly thanks CNES for the long term support of the 4A/OP radiative transfer model, including the recent extension to short wavelengths.

References

Armante, R., Scott, N., Crevoisier, C., Capelle, V., Crepeau, L., Jacquinet, N., and Chédin, A.: Evaluation of spectroscopic databases through radiative transfer simulations compared to observations. Application to the validation of GEISA 2015 with IASI and TCCON, Journal of Molecular Spectroscopy, 327, 180–192, https://doi.org/10.1016/j.jms.2016.04.004, 2016.

August, T., Klaes, D., Schlüssel, P., Hultberg, T., Crapeau, M., Arriaga, A., O'Carroll, A., Coppens, D., Munro, R., and Calbet, X.: IASI on Metop-A: Operational Level 2 retrievals after five years in orbit, Journal of Quantitative Spectroscopy and Radiative Transfer, 113, 1340–1371, https://doi.org/10.1016/j.jqsrt.2012.02.028, 2012.

Capelle, V., Chédin, A., Siméon, M., Tsamalis, C., Pierangelo, C., Pondrom, M., Crevoisier, C., Crepeau, L., and Scott, N. A.: Evaluation of IASI-derived dust aerosol characteristics over the tropical belt, Atmospheric Chemistry & Physics, 14, 9343–9362, https://doi.org/10.5194/acp-14-9343-201410.5194/acpd-13-30143-2013, 2014.

Capelle, V., Hartmann, J.-M., and Crevoisier, C.: A full physics algorithm to retrieve nighttime sea surface temperature with IASI: Toward an independent homogeneous long time-series for climate studies, Remote Sensing of Environment, 269, 112838, https://doi.org/10.1016/j.rse.2021.112838, 2022.

Cassé, V., Armante, R., Bousquet, P., Chomette, O., Crevoisier, C., Delahaye, T., Edouart, D., Gibert, F., Millet, B., Nahan, F., and Pierangelo, C.: Development and Validation of an End-to-End Simulator and Gas Concentration Retrieval Processor Applied to the MERLIN Lidar Mission, Remote Sensing, 13, 2679, https://doi.org/10.3390/rs13142679, 2021.

Cheruy, F., Scott, N. A., Armante, R., Tournier, B., and Chedin, A.: Contribution to the development of radiative transfer models for high spectral resolution observations in the infrared., Journal of Quantitative Spectroscopy and Radiative Transfer, 53, 597–611, https://doi.org/10.1016/0022-4073(95)00026-H, 1995.

Clerbaux, C., Boynard, A., Clarisse, L., George, M., Hadji-Lazaro, J., Herbin, H., Hurtmans, D., Pommier, M., Razavi, A., Turquety, S., Wespes, C., and Coheur, P.-F.: Monitoring of atmospheric composition using the thermal infrared IASI/MetOp sounder, Atmospheric Chemistry & Physics, 9, 6041–6054, https://doi.org/10.5194/acp-9-6041-200910.5194/acpd-9-8307-2009, 2009.

Crevoisier, C., Chédin, A., Matsueda, H., Machida, T., Armante, R., and Scott, N. A.: First year of upper tropospheric integrated content of CO_2 from IASI hyperspectral infrared observations, Atmospheric Chemistry & Physics, 9, 4797–4810, https://doi.org/10.5194/acp-9-4797-200910.5194/acpd-9-8187-2009, 2009.

Crevoisier, C., Nobileau, D., Armante, R., Crépeau, L., Machida, T., Sawa, Y., Matsueda, H., Schuck, T., Thonat, T., Pernin, J., Scott, N. A., and Chédin, A.: The 2007-2011 evolution of tropical methane in the mid-troposphere as seen from space by MetOp-A/IASI, Atmospheric Chemistry & Physics, 13, 4279–4289, https://doi.org/10.5194/acp-13-4279-201310.5194/acpd-12-23731-2012, 2013.

Delahaye, T., Armante, R., Scott, N. A., Jacquinet-Husson, N., Chédin, A., Crépeau, L., Crevoisier, C., Douet, V., Perrin, A., Barbe, A., Boudon, V., Campargue, A., Coudert, L. H., Ebert, V., Flaud, J.-M., Gamache, R. R., Jacquemart, D., Jolly, A., Kwabia Tchana, F., Kyuberis, A., Li, G., Lyulin, O. M., Manceron, L., Mikhailenko, S., Moazzen-Ahmadi, N., Müller, H. S. P., Naumenko, O. V., Nikitin, A., Perevalov, V. I., Richard, C., Starikova, E., Tashkun, S. A., Tyuterev, V. G., Vander Auwera, J., Vispoel, B., Yachmenev, A., and Yurchenko, S.: The 2020 edition of the GEISA spectroscopic database, Journal of Molecular Spectroscopy, 380, 111510, https://doi.org/10.1016/j.jms.2021.111510, 2021.

Dogniaux, M., Crevoisier, C., Armante, R., Capelle, V., Delahaye, T., Cassé, V., De Mazière, M., Deutscher, N. M., Feist, D. G., Garcia, O. E., Griffith, D. W. T., Hase, F., Iraci, L. T., Kivi, R., Morino, I., Notholt, J., Pollard, D. F., Roehl, C. M., Shiomi, K., Strong, K., Té, Y., Velazco, V. A., and Warneke, T.: The Adaptable 4A Inversion (5AI): description and first X_{CO_{2}} retrievals from Orbiting Carbon

Observatory-2 (OCO-2) observations, Atmospheric Measurement Techniques, 14, 4689–4706, https://doi.org/10.5194/amt-14-4689-2021, 2021.

Fletcher, L. N., Cavalié, T., Grassi, D., Hueso, R., Lara, L. M., Kaspi, Y., Galanti, E., Greathouse, T. K., Molyneux, P. M., Galand, M., Vallat, C., Witasse, O., Lorente, R., Hartogh, P., Poulet, F., Langevin, Y., Palumbo, P., Gladstone, G. R., Retherford, K. D., Dougherty, M. K., Wahlund, J.-E., Barabash, S., Iess, L., Bruzzone, L., Hussmann, H., Gurvits, L. I., Santolik, O., Kolmasova, I., Fischer, G., Müller-Wodarg, I., Piccioni, G., Fouchet, T., Gérard, J.-C., Sánchez-Lavega, A., Irwin, P. G. J., Grodent, D., Altieri, F., Mura, A., Drossart, P., Kammer, J., Giles, R., Cazaux, S., Jones, G., Smirnova, M., Lellouch, E., Medvedev, A. S., Moreno, R., Rezac, L., Coustenis, A., and Costa, M.: Jupiter Science Enabled by ESA's Jupiter Icy Moons Explorer, Space Science Reviews, 219, 53, https://doi.org/10.1007/s11214-023-00996-6, 2023.

Grassi, D., Adriani, A., Moriconi, M. L., Ignatiev, N. I., D'Aversa, E., Colosimo, F., Negrão, A., Brower, L., Dinelli, B. M., Coradini, A., and Piccioni, G.: Jupiter's hot spots: Quantitative assessment of the retrieval capabilities of future IR spectro-imagers, Planetary and Space Sciences, 58, 1265–1278, https://doi.org/10.1016/j.pss.2010.05.003, 2010.

Guérin, C.-A., Capelle, V., and Hartmann, J.-M.: Revisiting the Cox and Munk wave-slope statistics using IASI observations of the sea surface, Remote Sensing of Environment, 288, 113508, https://doi.org/10.1016/j.rse.2023.113508, 2023.

Haffoud, P., Poulet, F., Vincendon, M., Filacchione, G., Barbis, A., Guiot, P., Lecomte, B., Langevin, Y., Piccioni, G., Dumesnil, C., Rodriguez, S., Carter, J., Stefania, S., Tommasi, L., Tosi, F., and Pilorget, C.: Calibration of MAJIS (Moons And Jupiter Imaging Spectrometer). III. Spectral calibration, Review of Scientific Instruments, 95, 031301, https://doi.org/10.1063/5.0188944, 2024.

Jacquinet-Husson, N., Armante, R., Scott, N. A., Chédin, A., Crépeau, L., Boutammine, C., Bouhdaoui, A., Crevoisier, C., Capelle, V., Boonne, C., Poulet-Crovisier, N., Barbe, A., Chris Benner, D., Boudon, V., Brown, L. R., Buldyreva, J., Campargue, A., Coudert, L. H., Devi, V. M., Down, M. J., Drouin, B. J., Fayt, A., Fittschen, C., Flaud, J.-M., Gamache, R. R., Harrison, J. J., Hill, C., Hodnebrog, Ø., Hu, S.-M., Jacquemart, D., Jolly, A., Jiménez, E., Lavrentieva, N. N., Liu, A.-W., Lodi, L., Lyulin, O. M., Massie, S. T., Mikhailenko, S., Müller, H. S. P., Naumenko, O. V., Nikitin, A., Nielsen, C. J., Orphal, J., Perevalov, V. I., Perrin, A., Polovtseva, E., Predoi-Cross, A., Rotger, M., Ruth, A. A., Yu, S. S., Sung, K., Tashkun, S. A., Tennyson, J., Tyuterev, V. G., Vander Auwera, J., Voronin, B. A., and Makie, A.: The 2015 edition of the GEISA spectroscopic database, Journal of Molecular Spectroscopy, 327, 31–72, https://doi.org/10.1016/j.jms.2016.06.007, 2016.

Langevin, Y., Rodriguez, S., Guerlet, S., Poulet, F., Piccioni, G., Agostini, L., Armante, R., D'Aversa, E., Filacchione, G., Fletcher, L., Oliva, F., Royer, C., Seignovert, B., Stephan, K., Tosi, F., and Trent, T.: Post launch spectral and radiometric performances of MAJIS, the VIS-NIR imaging spectrometer of JUICE, Annales Geophysicae, 44, 825–853, https://doi.org/10.5194/angeo-44-825-2026, 2026.

Larar, A. M., Smith, W. L., Zhou, D. K., Liu, X., Revercomb, H., Taylor, J. P., Newman, S. M., and Schlüssel, P.: IASI spectral radiance validation inter-comparisons: case study assessment from the JAIVEx field campaign, Atmospheric Chemistry & Physics, 10, 411–430, https://doi.org/10.5194/acp-10-411-201010.5194/acpd-9-10193-2009, 2010.

Masuda, K.: Infrared sea surface emissivity including multiple reflection effect for isotropic Gaussian slope distribution model, Remote Sensing of Environment, 103, 488–496, https://doi.org/10.1016/j.rse.2006.04.011, 2006.

Masuda, K., Takashima, T., and Takayama, Y.: Emissivity of pure and sea waters for the model sea surface in the infrared window regions, Remote Sensing of Environment, 24, 313–329, https://doi.org/10.1016/0034-4257(88)90032-6, 1988.

Oliva, F., D'Aversa, E., Migliorini, A., Piccioni, G., Poulet, F., Langevin, Y., Filacchione, G., Ciarniello, M., Rodriguez, S., Seignovert, B., Mura, A., Fletcher, L. N., Zinzi, A., Giardino, M., Lopinto, E., Sindoni, G., and Plainaki, C.: JUICE-MAJIS Earth observations during the

2024 gravity assist: first analysis and comparison with PRISMA data, EGUsphere, 2026, 1–51, https://doi.org/10.5194/egusphere-2025-6455, 2026.

Phulpin, T., Blumstein, D., Prel, F., Tournier, B., Prunet, P., and Schlüssel, P.: Applications of IASI on MetOp-A: first results and illustration of potential use for meteorology, climate monitoring, and atmospheric chemistry, in: Atmospheric and Environmental Remote Sensing Data Processing and Utilization III: Readiness for GEOSS, edited by Goldberg, M. D., Bloom, H. J., Huang, A. H., and Ardanuy, P. E., vol. 6684 of *Society of Photo-Optical Instrumentation Engineers (SPIE) Conference Series*, p. 66840F, https://doi.org/10.1117/12.736816, 2007.

Poulet, F., Piccioni, G., Langevin, Y., Dumesnil, C., Tommasi, L., Carlier, V., Filacchione, G., Amoroso, M., Arondel, A., D'Aversa, E., Barbis, A., Bini, A., Bolsée, D., Bousquet, P., Caprini, C., Carter, J., Dubois, J.-P., Condamin, M., Couturier, S., Dassas, K., Dexet, M., Fletcher, L., Grassi, D., Guerri, I., Haffoud, P., Larigauderie, C., Le Du, M., Mugnuolo, R., Pilato, G., Rossi, M., Stefani, S., Tosi, F., Vincendon, M., Zambelli, M., Arnold, G., Bibring, J.-P., Biondi, D., Boccaccini, A., Brunetto, R., Carapelle, A., Cisneros González, M., Hannou, C., Karatekin, O., Le Cle'ch, J.-C., Leyrat, C., Migliorini, A., Nathues, A., Rodriguez, S., Saggin, B., Sanchez-Lavega, A., Schmitt, B., Seignovert, B., Sordini, R., Stephan, K., Tobie, G., Zambon, F., Adriani, A., Altieri, F., Bockelée, D., Capaccioni, F., De Angelis, S., De Sanctis, M.-C., Drossart, P., Fouchet, T., Gérard, J.-C., Grodent, D., Ignatiev, N., Irwin, P., Ligier, N., Manaud, N., Mangold, N., Mura, A., Pilorget, C., Quirico, E., Renotte, E., Strazzulla, G., Turrini, D., Vandaele, A.-C., Carli, C., Ciarniello, M., Guerlet, S., Lellouch, E., Mancarella, F., Morbidelli, A., Le Mouélic, S., Raponi, A., Sindoni, G., and Snels, M.: Moons and Jupiter Imaging Spectrometer (MAJIS) on Jupiter Icy Moons Explorer (JUICE), Space Science Reviews, 220, 27, https://doi.org/10.1007/s11214-024-01057-2, 2024.

Poulet, F., Piccioni, G., Langevin, Y., Dumesnil, C., Carlier, V., Seignovert, B., Dexet, M. a nd N. Fletcher, L., Leyrat, C., Altieri, F., Carter, J., D'Aversa, E., De Sanctis, M., Grassi, D., Gu erlet, S., Le Mouélic, S., Migliorini, A., Oliva, F., Royer, C., Rodriguez, S., Stephan, K., Tosi, F., Zambon, F., Adriani, A., Arnold, G., Bibring, J.-P., Bockelée, D., Brunetto, R., Capaccioni, F., Carli, C., Cavalié, T., Cisneros González, M., Ciarnello, M., De Angelis, S., Drossart, P., Fil acchione, G., Fouchet, T., Gérard, J.-C., Grodent, D., Irwin, P., Jacquinod, S., Karatekin, O., Lel louch, E., Ligier, N., Mangold, N., Mebsout, M., Merlin, F., Morbidelli, A., Mura, A., Nathues, A. an d E. Palumbo, M., Pilorget, C., Poch, O., Quirico, E., Raponi, A., Robert, S., Roussos, E., Sanchez-L avega, A., Schmitt, B., Sindoni, G., Snels, M., Sordini, R., Stefani, S., Strazzulla, G., Trent, T. a nd Tobie, G., Turrini, D., Vandaele, A.-C., Vincendon, M., Witasse, O., Vallat, C., and Moraino, A.: ESA/JUICE encounters Earth/Moon in 2024: overview of the Moons And Jupiter Imaging Spectrometer (MAJIS) observati ons, EGUsphere, 2025, 1–58, https://doi.org/10.5194/egusphere-2025-6191, 2025.

Scott, N. A. and Chedin, A.: A fast line-by line method for atmospheric absorption computations: the Automatized Atmospheric Absorption Atlas., Journal of Applied Meteorology, 20, 802–812, https://doi.org/10.1175/1520-0450(1981)020<0802:AFLBLM>2.0.CO;2, 1981.

Sic, B., Jacquette, E., Jouglet, D., Lafrique, P., Pierangelo, C., Armante, R., Lezeaux, O., and Hajj, M. E.: Implementation of low stream interpolation technique to accelerate scattering calculations in the 4A/OP radiative transfer model, Journal of Quantitative Spectroscopy and Radiative Transfer, 349, 109734, https://doi.org/10.1016/j.jqsrt.2025.109734, 2026.

Whitburn, S., Clarisse, L., Crapeau, M., August, T., Hultberg, T., Coheur, P. F., and Clerbaux, C.: A CO_2-independent cloud mask from Infrared Atmospheric Sounding Interferometer (IASI) radiances for climate applications, Atmospheric Measurement Techniques, 15, 6653–6668, https://doi.org/10.5194/amt-15-6653-2022, 2022.